Asian Journal of Chemistry; Vol. 37, No. 1 (2025), 123-134

ASIAN JOURNAL OF CHEMISTRY

https://doi.org/10.14233/ajchem.2025.32904

Enhancing Photocatalytic Degradation of Methylene Blue and Malachite Green under Solar Light Irradiation: Mechanistic Insights and Efficiency of $BiVO_4$ and Sr-Doped $BiVO_4$ Nanoparticles

PRAFULLA KUMAR PANDA, RISHABH KAMAL, RASMIREKHA PATTANAIK, DEBAPRIYA PRADHAN and SURESH KUMAR DASH*

Department of Chemistry, ITER, Siksha 'O' Anusandhan (Deemed to be University), Bhubaneswar-751030, India

*Corresponding author: E-mail: sureshdash@soa.ac.in

Received: 16 October 2024; *Accepted*: 6 December 2024; *Published online*: 31 December 2024; AJC-21859

Water pollution from untreated dye discharge has become a significant concern for all living organisms and the treatment of polluted water has become a priority. In this study, a monoclinic–tetragonal hetero-structured $BiVO_4$ and strontium doped (15, 20 and 25 wt.%) $BiVO_4$ NPs were synthesized using a simple co-precipitation method. The structural, optical and morphological properties of the catalysts were characterized using XRD, FTIR, UV-DRS, FESEM, TEM, PL and BET analysis. The XRD pattern exhibited the retentions of crystalline structure of $BiVO_4$ after Sr doping. The Sr-$BiVO_4$ exhibited a reduced band gap energy of 2.3 eV, significantly lower than that of the pristine $BiVO_4$. Additionally, Sr-$BiVO_4$ had an increased surface area of 16.2 m^2/g nearly twice that of the pristine material. Photocatalytic activities of the prepared samples were evaluated with changing parameters such as pH, initial concentration, catalyst dose and agitation time towards the degradation of methylene blue (MB) and malachite green (MG) dyes under solar light irradiation. The results showed that Sr-$BiVO_4$ achieved a degradation efficiency of 91% for methylene blue and 94% for malachite green at pH ~ 9 with a 20 mg catalyst dose in 120 min. The dye degradation followed a pseudo-first-order kinetic model and the catalyst demonstrated an excellent stability even after five consecutive runs. The active species test carried out using *p*-benzoquinone, isopropyl alcohol and Na-EDTA revealed that superoxide radicals played a key role in the degradation mechanism.

Keywords: Sr-$BiVO_4$, Methylene blue, Malachite green dyes, Photodegradation, Kinetic studies, Recyclability, Active species.

INTRODUCTION

Clean and safe water is the sine qua non for survival of living beings on this planet [1,2]. As a result of unplanned urbanization, human population explosion, rapid industrialization effluents are discharged directly to waterbodies causing enormous amount of water pollution [3]. Different industries like textiles, mining, pharmaceuticals also release wastewater in large quantities directly to the environment [4]. For the purpose of removing pollutants and guaranteeing compliance with the environmental regulations, efficient water and wastewater treatment is essential. One of the primary contributors to these hazardous pollutants is the excessive usage of dyes [5]. Due to toxic, carcinogenic and mutagenic nature, organic dyes are harmful for living organisms and they have adverse effects on human and animal health [6]. Though different methods like coagulation, adsorption, ion-exchange, sedimentation and ultrafiltration are available for dye removal, these are inadequate and expensive and result in additional contamination or simply transfer pollutants from one phase to another [2-7].

On the contrary, heterogeneous photocatalysis as an efficient water treatment process has gained attention in recent years to meet the global challenges related to environment, energy and sustainability because of several advantages such as no waste byproducts, eco-friendliness, low cost and completely mineralization [8]. Toxic organic compounds can be destroyed quite successfully by using photocatalysts made of nanostructured semiconductors [9]. Nanocomposites consisting of various semiconductors have the capability to customize the band gap of photocatalysts, expanding the range of photo-response and the generation of electron-hole pairs, thereby improving the photo-catalytic efficiency in the degradation of organic pollutants. The alignment of band edges in the photocatalysts could mitigate the recombination of electron-hole pairs. Numerous studies have been dedicated to investigating mixed nanocomposites for their potential in catalytic applications [10].

TiO_2, ZnO and WO_3 have greater band gap energies and poor visible light absorption, whereas binary oxide semiconductors have poor charge transport characteristics (Fe_2O_3) and stability (Cu_2O), limiting their practical usage as photocatalysts. However, the high band gap and electron hole recombination are the main limitations of these photocatalysts, lowering their photocatalytic effectiveness. Moreover, they absorb roughly 2-3% of the solar spectrum while staying active in the ultraviolet region [11]. As a result, the quest for effective photocatalysts is in high demand. The most significant properties of an effective photocatalyst are a wide surface area, a narrow band gap, quick charge carrier transformation and the capacity to absorb solar radiation within the visible region. $BiVO_4$, an n-type semiconductor, is the ideal alternative due to its low band gap (2.4 eV), non-toxicity, corrosion resistance, stability and superior dispensability [12,13]. $BiVO_4$ consists of three crystal phases *viz.* monoclinic scheelite, tetragonal zircon and tetragonal scheelite [14-16]. Out of them, monoclinic $BiVO_4$ has a band gap of 2.4 eV, making it a potential visible light photocatalyst for dye degradation [16,17]. $BiVO_4$ is synthesized through a variety of processes, including hydrothermal, co precipitation, template assisted and sol-gel [18-22]. The efficiency of $BiVO_4$ has been much below expectations due to its weak electron-hole separation yield.

Therefore, by altering the band structure through doping or the formation of a composite with other materials like metal, metal oxide, polymeric materials and non-metals, its efficiency can be further increased. Doping improves the catalytic activity of $BiVO_4$ composite by reducing its band-gap and shifting the band between the valence and conduction bands [23]. A practical strategy to enhance the efficacy of semiconductor photocatalysts in degrading organic pollutants is the integration of rare metals. This is accomplished by improving the light absorption by introducing intra-band gap states and decreasing the band gap and recombination efficiency of electron-hole pairs produced by light. Research has shown that through the process of up-conversion, the presence of rare metals can greatly increase the photocatalytic efficiency of semiconductors. This process makes it easier to convert low-energy incident light into higher-energy emitted light because it exhibits a nonlinear optical response [24]. Metal-doped $BiVO_4$ photocatalysts have attracted considerable interest in the realm of photocatalysis for their superior efficiency in breaking down organic contaminants and producing hydrogen *via* water splitting. The incorporation of noble metals such as Au, Ag, Pt and Pd onto the $BiVO_4$ surface significantly improves the photocatalytic activity. The metal modification of $BiVO_4$ photocatalysts can also involve other metals like Ag, Pt and Pd, each offering unique advantages in terms of charge separation, active site generation and plasmonic effects [25-28]. These modifications aim to address the limitations of pristine $BiVO_4$, such as its inefficient quantum yield and low visible-light response, thereby improving the overall photocatalytic efficiency. These modifications result in the synergistic effects that significantly boost the efficiency of $BiVO_4$ in degrading organic pollutants in water treatment processes. Furthermore, metal-modified $BiVO_4$ exhibits long-term stability and enhanced photocatalytic activity, making it a promising candidate for sustainable and efficient water treatment applications.

Strontium, one of the alkaline earth metals, has been used as a dopant in numerous semiconductors. So, to increase photocatalytic efficiency, strontium is doped with $BiVO_4$. The present study describes a straightforward co-precipitation approach for synthesizing $BiVO_4$ nanoparticles and Sr doped $BiVO_4$ nanoparticles. Both are used to photodegrade the poisonous dyes methylene blue and malachite green dyes under sunlight irradiation.

EXPERIMENTAL

$Bi(NO_3)_3·5H_2O$, NH_4VO_3 and NaOH (all procured from Merck) have been used at 99% purity. High purity acetic acid was added to HNO_3. Deionized double distilled water has been used to prepare the solution.

Synthesis of $BiVO_4$: An easy co-precipitation process led to the formation of $BiVO_4$. The bismuth and vanadium precursors, namely bismuth nitrate pentahydrate [$Bi(NO_3)_3·5H_2O$] and ammonium metavanadate (NH_4VO_3) in a 1:1 molar ratio, were mixed in 1 M nitric acid solution. After the formation of reddish-yellow colour, a 1 M NaOH solution was slowly introduced with vigorous agitation to elevate the pH to 10. The resulting pale yellow solution was centrifuged and rinsed with distilled water thoroughly. After drying in oven for 3 h, the filtrate was calcined in a muffle furnace at 500 ºC. The yellow-coloured material was finely pulverized and collected.

Synthesis of Sr doped $BiVO_4$: Using a co-precipitation technique, different percentages of strontium-doped $BiVO_4$ (15%, 20% and 25%) were obtained. A 100 mL aqueous solution containing 0.1 M $Bi(NO_3)_3·5H_2O$ and different concentrations of $Sr(NO_3)_2$ was produced and allowed to agitate at room temperature for 30 min. After that, 10 mL ammonia/ethanol solution was added dropwise to the first solution and then vigorously stirred for 0.5 h. In the same vessel, the manufactured gel was aged for the entire night. The following day, the precipitate was filtered and repeatedly washed with water to order to remove excess ethanol and ammonia.

The remaining bulk was calcined for 3 h at 650 ºC after being dried for 5 h at 100 ºC in an oven. Sr–$BiVO_4$, the material that had been calcined, was ground into a fine powder and employed for further experiments. Sr(x)–$BiVO_4$ was the label applied to the manufactured nanocomposite materials ($x = 15$, 20 and 25).

Characterization: The crystalline structure of the samples was analyzed using a powder X-ray diffractometer (Philips PW 1830, Japan) employing ($CuK\alpha$) radiation, with the 2θ angle scanned from 10º to 80º, X-ray diffraction (XRD) was utilized to examine the crystalline architecture and surface topography of $BiVO_4$ nanoparticles. Using a transmission electron microscope (TEM) Jeol/JEM 2100 and a field emission scanning electron microscope (FE-SEM) ZEISS SUPRA 55, the textural characteristics were investigated. The elemental composition was determined using EDS technique. Fourier-transform infrared (FTIR) spectroscopy, performed using a Perkin-Elmer Spectrum instrument (version 10.4.3), was employed to identify the characteristic vibrational modes of $BiVO_4$ nanoparticles and a UV-DRS spectrophotometer (Perkin-Elmer Lamda 365) was used to examine the optical properties. The specific surface area and pore size distribution of the $BiVO_4$ samples were determined using a nitrogen adsorption-desorption analyzer (Quantachrome Instruments v11.05). A UV-vis spectrophotometer (Sys TM 2202) was employed to quantify the concentration of methylene blue (MB) and malachite green (MG) solutions before and after the photocatalytic degradation experiments.

Photocatalytic analysis: Using bismuth vanadate ($BiVO_4$) and strontium-doped bismuth vanadate (x)Sr-$BiVO_4$ nanoparticles as catalysts, the photocatalytic degradation process of both methylene blue (MB) and malachite green (MG) dyes was studied. The photocatalytic efficiency of the $BiVO_4$-based materials was evaluated under varying conditions *viz.* initial dye concentration (20, 40, 60 and 80 ppm), solution pH (3, 5, 7, 9 and 11), photocatalyst dosage (10, 20, 30, 40 and 50 mg) and contact time (30, 60, 90, 120 and 150 min), to identify the optimal parameters for enhanced pollutant degradation. From February to June, the study was conducted under direct sunlight with a solar insolation of 3000 Wh/m^2. Variations in pH, catalyst dosage, agitation time and starting concentration all enhanced the efficacy of the photocatalytic process. Deionized water (1 L) was used to dissolve 0.1 g of methylene blue and malachite green to obtain 100 ppm stock solutions. Then, as per requirement, this solution was diluted to 20, 40, 60 and 80 ppm. During the photocatalytic evaluation, a 100 mL conical flask was utilized to mix 25 mL of specified concentration solution with the appropriate quantity of catalyst. The pH of the solutions was altered either by adding 0.01 M CH_3COOH or NH_4OH solutions. The resulting mixture was shaken in dark for 0.5 h in order to investigate the adsorption-desorption equilibrium. Following exposure to solar irradiation, the reaction mixture was shielded with an asbestos pad to prevent the intrusion of UV light. The reaction mixture was then subjected to stirring, followed by centrifugation and filtration to separate the photocatalyst from the solution. To study the photocatalytic degradation process, the filtrate was collected. Subsequently, the concentration of the degraded dyes was determined using a UV-Vis spectrophotometer at the respective absorbance wavelengths (662 nm for methylene blue and 616 nm for malachite green). The kinetics of the photodegradation of the dyes were studied by measuring small volumes of each solution at 30, 60, 90 and 120 min intervals.

Quenching experiment: In order to capture the reactive species produced during the photocatalytic process, solutions of several quenchers, such as isopropanol for hydroxyl radicals, *p*-benzoquinone for superoxide radicals and silver nitrate for electrons, were obtained for the quenching experiment. The setup for the experiment was same as for the photocatalytic tests. In brief, a 100 mL conical flask was charged with 25 mL of dye solution at the desired concentration, followed by the addition of catalyst. The pH of solution was changed as necessary. The dye solution was then mixed with a certain volume of the quencher solution and the volume was varied to study the effect of quencher concentration on the photocatalytic process.

The mixture was agitated for 30 min in dark in order to achieve equilibrium between adsorption and desorption. After that, the mixture was exposed to solar light and covered to stop UV radiation from penetrating. Periodically, small samples of each solution (30, 60, 90, 120 and 150 min) were obtained for analysis. The concentration of the dyes after degradation was quantified using a UV-vis spectrophotometer at the characteristic absorbance wavelengths. The significance of various reactive species in the photocatalytic process was determined by comparing degradation rates with and without the quenchers.

Recyclability studies: Centrifugation was used to remove the $BiVO_4$ and (x)Sr-$BiVO_4$ nanoparticles from the solution following the quenching process. Then, the collected nanoparticles were repeatedly washed with ethanol and deionized water to remove any remaining dye. For reuse, the cleaned $BiVO_4$ nanoparticles were dried for 12 h at 60 ºC. In a similar setting, a new cycle of photocatalytic degradation of methylene blue and malachite green dyes was carried out, employing the dried nanoparticles as catalyst. To demonstrate the efficiency after five runs, the stability and recyclability of photocatalyst were examined. After every cycle, the tests were conducted in the same settings as described above.

RESULTS AND DISCUSSION

XRD studies: The phase of crystallization is ascertained by X-ray diffraction analysis, as the XRD patterns of $BiVO_4$ as shown in Fig. 1. The identified diffraction peaks at 2θ values of 18.6º, 28.7º, 34.5º, 35.2º, 39.5º, 45.7º, 46.9º, 49.9º, 53.2º, 55.7º, 58.2º and 59.0º correspond to (001), (013), (004), (200), (020), (211), (015), (123), (204) and (59.0). Each peak corresponds to the monoclinic structure of $BiVO_4$ (JCPDS No. 83-1699). The Debye-Scherrer's equation, as shown in eqn. 1, was applied to calculate the particle size of $BiVO_4$ nanoparticles, resulting in a size of 34.8 nm [8].

$$D = \frac{K\lambda}{\beta \cos\theta} \quad (1)$$

where K represents Scherrer's constant (K = 0.94); λ is the X-ray wavelength (1.54178 Å); β denotes the full-width at half-maximum (FWHM) of the diffraction peak and θ corresponds to the Bragg angle of the respective peak [29].

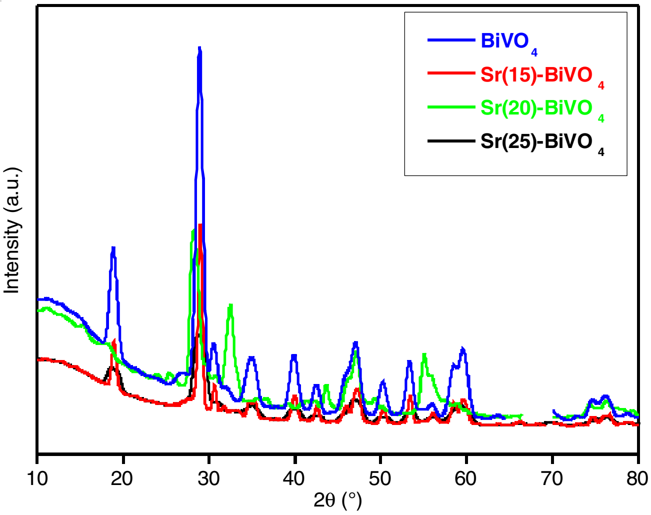

Fig. 1. XRD patterns of $BiVO_4$ and (*x*)Sr-$BiVO_4$ (where *x* = 15, 20 and 25 wt.%)

When comparing the diffraction peaks of pure $BiVO_4$ to those of Sr-doped $BiVO_4$ at different concentrations (Sr(15%)-$BiVO_4$, Sr(20%)-$BiVO_4$, Sr(25%)-$BiVO_4$), it is evident that the peaks shift to lower 2θ angles in the doped samples. This shift suggests an increase in the lattice parameters, likely due to the incorporation of larger Sr^{2+} ions into the $BiVO_4$ lattice, which causes an expansion of the unit cell [30,31].

FTIR studies: The symmetric and asymmetric stretching vibrations at 900-700 cm^{-1} is attributed due to the V-O bond [11,27], as depicted in Fig. 2. The prominent absorption bands at 3410 cm^{-1} and 1600 cm^{-1} are attributed to the H-O-H stretching and bending vibrations, respectively, corresponding to the presence of adsorbed water molecules on the catalyst surface. The Bi-O stretching vibration of the band is indicated by the peak at 532 cm^{-1} [32]. The absorption bands at 3410 cm^{-1} and 1600 cm^{-1} in the FTIR spectrum of strontium-doped bismuth vanadate ($BiVO_4$) may not solely indicate the H-O-H stretching and bending vibrations but could also be attributed to other impurities or structural characteristics of $BiVO_4$. Studies have shown that different dopants and synthesis methods can introduce variations in the FTIR spectra of $BiVO_4$, potentially leading to the overlapping peaks that might be mistaken for specific functional groups. Additionally, the presence of impurities or mixed phases, as observed in various synthesis routes like laser ablation, sol-gel and solid-state methods, can also contribute to additional peaks in the FTIR spectrum, complicating the interpretation of vibrational modes [33-37]. Therefore, when analyzing FTIR spectra of doped $BiVO_4$ materials, it is crucial to consider the influence of dopants, impurities and structural variations to accurately assign vibrational bands and understand the material's composition.

UV-DRS spectral studies: Fig. 3a displays the UV-DRS spectra of $BiVO_4$, which demonstrate the catalyst's capacity to both generate strong photocatalytic activity and absorb visible light. The catalyst exhibits a significant absorption peak between 300 and 420 nm. The tauc plot is represented as follows:

$$(\alpha h\nu)^{1/2} = A\,(h\nu - E_g)^n \qquad (2)$$

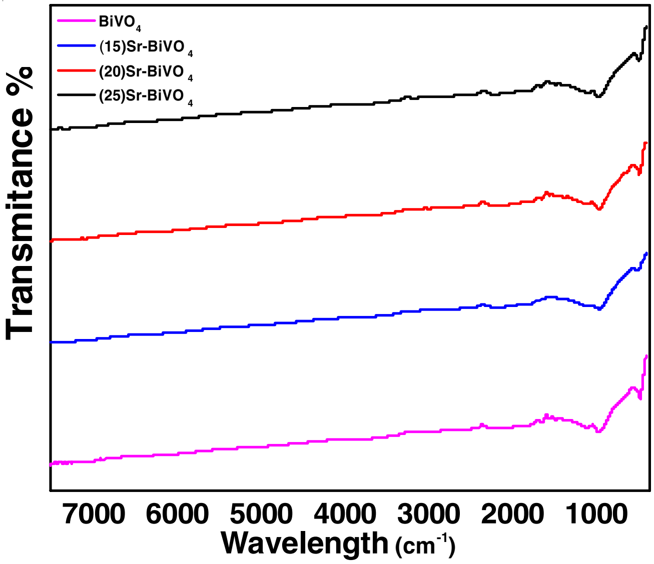

Fig. 2. FTIR spectra of undoped $BiVO_4$ and (*x*)Sr-doped $BiVO_4$ (where *x* = 15, 20 and 25 wt.%)

where α is the absorption coefficient; A is the constant; and n control the change from indirect (n = 2) to direct (n = 1/2). The calculation of the band gap energy (E_g) involves projecting the linear portion of the $(\alpha h\nu)^{1/2}$ *versus* (hν) graph. Thus from the Tauc plot (Fig. 3b), the band gap energy of $BiVO_4$ was found to be 2.3 eV [38].

The procedure consists of initially computing the absorption coefficient (α) from the UV-Vis absorbance measurements. Following this, the plot of (αhν)n against hν is constructed, with n being 1/2 for direct transitions and 2 for indirect transitions. A linear regression analysis is then employed in the most linear segment of the graph and extending this linear fit to the *x*-axis (photon energy axis) yields the band gap energy. Direct transitions entail a direct recombination of electrons and holes with minimal momentum alteration (n = 1/2), whereas indirect transitions involve phonon interactions, resulting in greater momentum changes (n = 2). Research findings have shown that $BiVO_4$

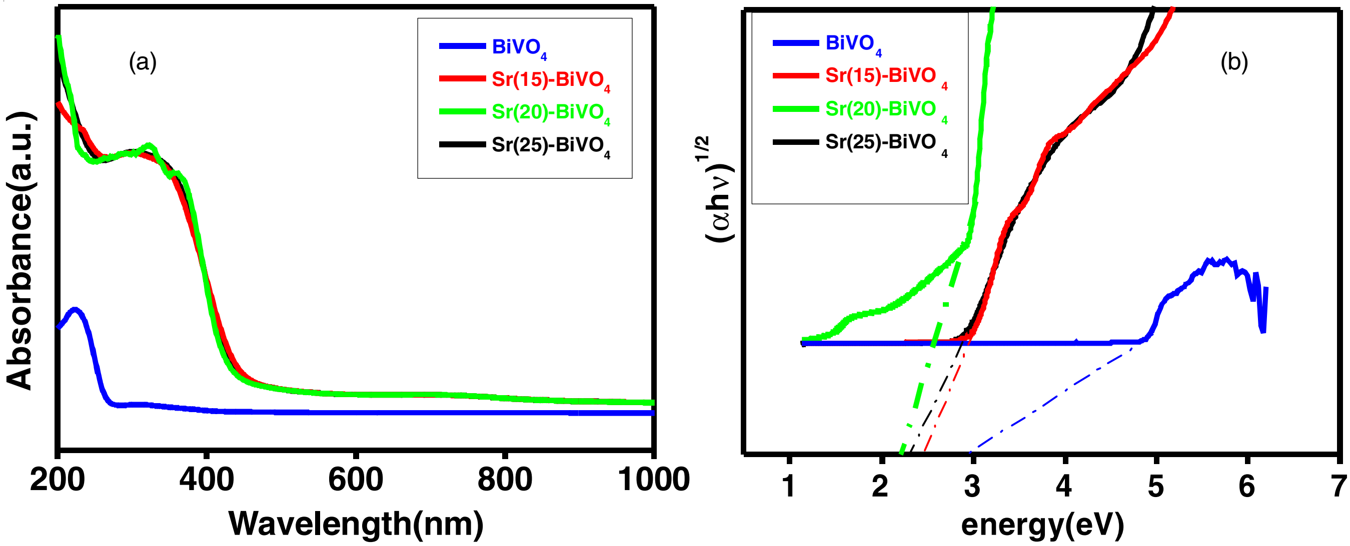

Fig. 3. (a) UV-DRS spectra of undoped $BiVO_4$ (blue) and (*x*) Sr-doped $BiVO_4$ (where *x* = 15, 20 and 25 wt.%) and (b) determination of band gap energy for undoped $BiVO_4$ (blue) and (*x*)Sr-doped $BiVO_4$ (where *x* = 15, 20 and 25 wt.%) from Tauc plot

displays an indirect band gap, as indicated by the linearity observed in the $(\alpha h\nu)^2$ *versus* $h\nu$ plot, thereby confirming a band gap energy of 2.3 eV [39,40].

Doping can significantly enhance light absorption in $BiVO_4$ by introducing new energy levels within the band gap, thereby improving the light absorption capabilities of the material. When dopants like tungsten or molybdenum are incorporated into the $BiVO_4$ lattice, they create shallow donor levels–energy states situated just below the conduction band [41]. These levels facilitate the excitation of electrons into the conduction band upon light absorption, increasing charge carrier density and enhancing photocatalytic activity. Additionally, doping induces changes in the band structure of $BiVO_4$, altering the positions of the valence band maximum (VBM) and conduction band minimum (CBM), which effectively modifies the band gap energy (E_g). A reduced band gap enables the material to absorb a wider spectrum of light, including visible light, crucial for photocatalytic applications. Furthermore, doping improves the separation of photogenerated electron-hole pairs by creating an electric field in the space-charge region, thereby reducing recombination rates and allowing more electrons to participate in photocatalytic reactions. Experimental evidence shows that doped $BiVO_4$ exhibits improved photocurrent responses under light irradiation compared to undoped samples, with Sr-doped $BiVO_4$ demonstrating higher photocurrent densities, indicative of enhanced light absorption and utilization [42].

Surface and morphological studies: The FESEM image of pure $BiVO_4$ revealed the aggregation of nanoparticles, comprising numerous irregular and smaller crystals. These primary particles were closely sintered together, resulting in the formation of larger aggregates. Incase of doped $BiVO_4$, the FESEM image showed the deposition of rectangular shape nanoparticles on the spherical shaped particles, which were due to doping of Sr indicating that the morphology of $BiVO_4$ is influenced by doping. The elemental composition of the materials was confirmed through EDX analysis, as shown in Fig. 4a. The EDX spectrum of pure $BiVO_4$ reveals the presence of Bi, V and O, indicating the high purity of the catalyst. For the Sr-modified $BiVO_4$, the detection of Sr, along with Bi, V and O, confirms the successful incorporation of Sr into the $BiVO_4$ lattice. The TEM image (Fig. 5) provides a clear visualization of the microstructural features of the $BiVO_4$ microspheres. The magnified TEM image of $BiVO_4$ having a diameter of 30 nm illustrates the uniformity and clarity.

Brunauer-Emmett-Teller (BET) studies: For $BiVO_4$, the specific surface area is 9.42 m^2/g and the pore diameter is 3.646 nm. On the other hand, for (20)Sr-$BiVO_4$, the specific surface area is 16.7 m^2/g and the pore diameter is 1.985 nm. This indicates that (20)Sr-$BiVO_4$ has a larger surface area per gram than $BiVO_4$, suggesting that strontium doping has increased the available surface for interaction (Fig. 6). This could potentially enhance its performance in applications where surface

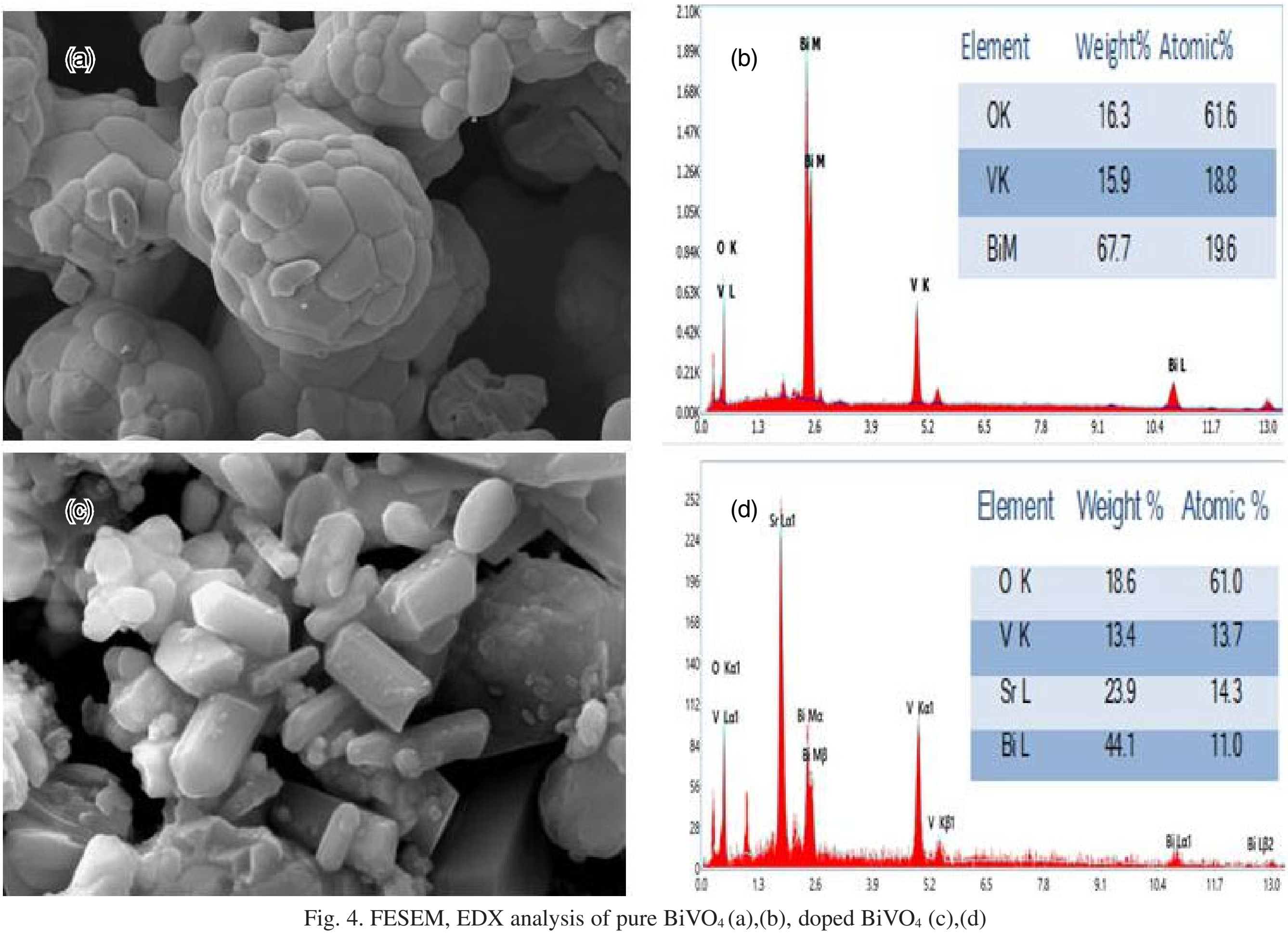

Element	Weight%	Atomic%
OK	16.3	61.6
VK	15.9	18.8
BiM	67.7	19.6

Element	Weight %	Atomic %
O K	18.6	61.0
V K	13.4	13.7
Sr L	23.9	14.3
Bi L	44.1	11.0

Fig. 4. FESEM, EDX analysis of pure $BiVO_4$ (a),(b), doped $BiVO_4$ (c),(d)

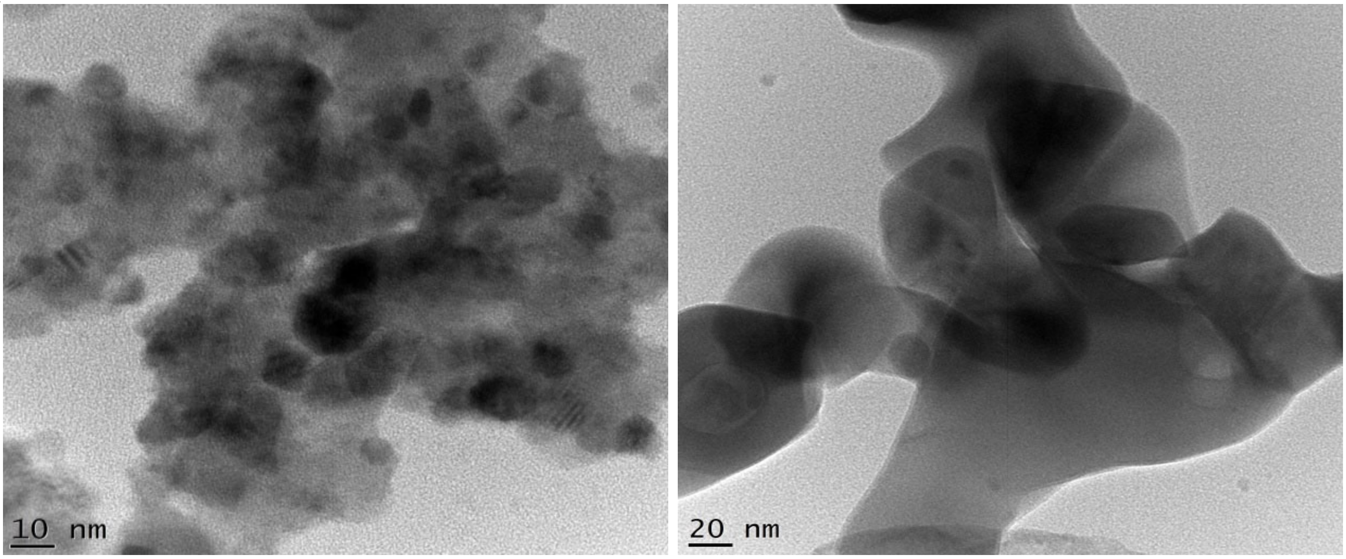

Fig. 5. TEM images of $BiVO_4$ microspheres and elemental composition in the sample

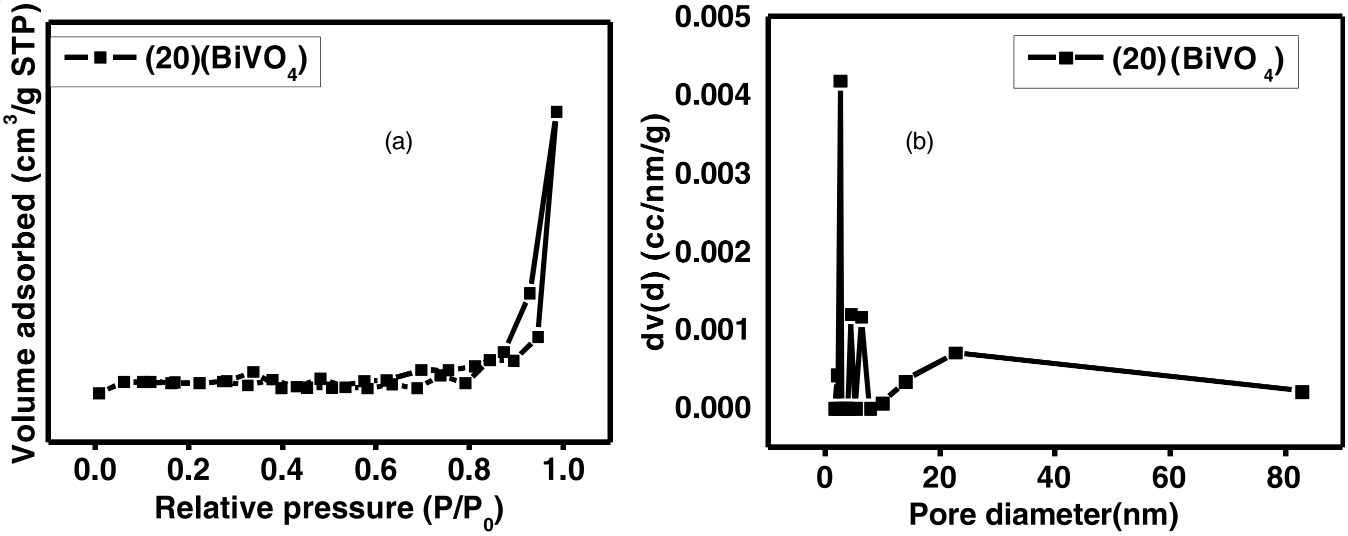

Fig. 6. (a) Doped (20) Sr-$BiVO_4$; N_2 adsorption/desorption isotherms and (b) BJH pore size of doped (20)Sr-$BiVO_4$

interactions are important. However, the pore diameter of (20)Sr-$BiVO_4$ is smaller than that of $BiVO_4$, which might influence the accessibility of these surfaces in applications involving larger molecules or particles [38].

Photoluminescence (PL) studies: The PL spectra of pure $BiVO_4$ and (20)Sr-$BiVO_4$ demonstrate the recombination, migration and transfer of photogenerated electron-hole pairs in semiconductors. The peaks were displayed in the figure at roughly 494 nm (Fig. 7). A higher rate of e^- and h^+ recombination is indicated by the intensity of pure $BiVO_4$, which is higher than that of Sr-doped $BiVO_4$. The lower intensity of (20)Sr-$BiVO_4$ suggests that Sr doping effectively prevented the excess e^-/h^+ pair recombination because increased charge carrier separation lowers the rate of electron-hole pair recombination and increases photocatalytic activity by involving more free charge carriers [43].

Photocatalytic studies: The assessment of the photocatalytic effectiveness of the produced $BiVO_4$ was conducted on the methylene blue (MB) and malachite green (MG) under

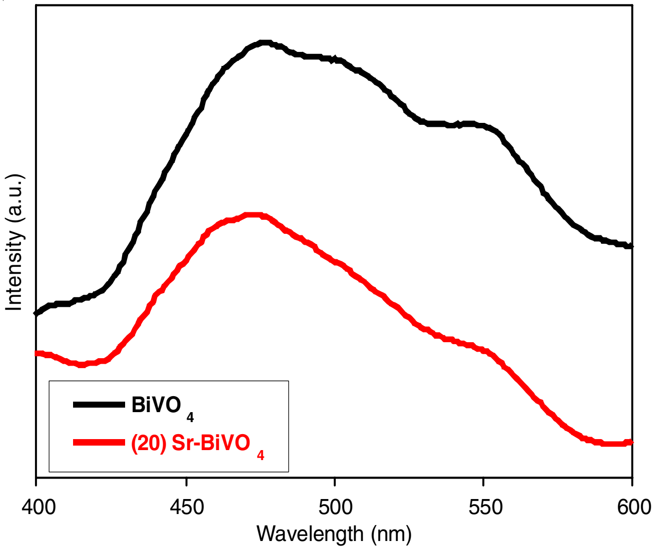

Fig. 7. PL spectra of undoped $BiVO_4$ (black) and (20)Sr-doped $BiVO_4$ (red)

solar radiation. Several aspects, including the pH of dye solution, the concentration of dye, the amount of catalyst and the time duration of radiation exposure, were taken into consideration in order to gain a thorough understanding of the elements impacting degradation efficiency.

Eqn. 3 was used to calculate the photocatalytic degradation efficiency of the catalyst towards methylene blue (MB) and malachite green (MG) dyes:

$$\text{Degradation (\%)} = \frac{C_0 - C_t}{C_0} \times 100 \tag{3}$$

where C_0 is the dye concentration at time t = 0; and C_t is the dye concentration at time t during agitation in the presence of a light source.

Influence of pH: In order to investigate the pH dependency, the degradation procedure was conducted across a range of pH values (3, 5, 7, 9 and 11). Adjustments to the pH of dye solution were made using dilute HCl or NaOH solution. Previous studies have reported that $BiVO_4$ exhibits a point of zero charge (pH_{pzc}) at approximately 3.5, implying that at this specific pH value, the catalyst surface carries a neutral charge. The surface charge of catalyst is negative above pH 3.5 and positive below pH 3.5 [15]. Fig. 8 shows the percentage of degradation for both methylene blue and malachite green. The pH values lower than 9, highest degradation rates of 91% and 94% have been attained for methylene blue and malachite green, respectively. Dye degradation is the result of the maximum degradation caused by the negatively charged surface of $BiVO_4$ above pH 3.4 at an alkaline pH [17].

Influence of initial dye concentration: The effect of varied methylene blue and malachite green dyes (20, 40 and 60 ppm) concentrations on degrading effectiveness was also examined while keeping the $BiVO_4$ dose at 20 mg and pH 9. The methylene blue and malachite green had the highest percentage of dye degradation at 20 ppm, with 94% and 98%, respectively. The efficiency of degradation decreased with increasing concentration, attributed to the excess of dye molecules acting as barriers between solar light and catalytic surfaces, thereby hindering the generation of charge carriers and resulting in reduced performance [44].

Influence of catalyst dose: The photocatalytic degradation was investigated using different catalyst loadings of 10, 20 and 30 mg of $BiVO_4$ per 100 mL of dye solution, while maintaining a constant pH of 9 and an initial dye concentration of 20 ppm for both methylene blue (MB) and malachite green (MG) dyes. As seen in Fig. 9, the highest degradation rate of 93.2% of methylene blue and 97.1% of malachite green was observed at 20 mg of catalyst; however, this rate declined as the catalyst dose was increased. The degradation rate increased as a result of the availability of additional active sites. Nevertheless, overcrowding caused a collision of catalyst particles after 20 mg of catalyst for methylene blue and malachite green, which decreased the formation of charge carriers and slowed the rate of degradation [45].

Influence of time: The dye solution containing a specific amount of $BiVO_4$ was shaken in solar light for 120 min to confirm the impact of agitation time. The during the degradation process, the UV-Vis analysis was conducted at the intervals of 20 min. The maximum degradation of 95.3% and 96.7 % for methylene blue and malachite green was reached in 120 min. At the beginning of agitation period of up to 120 min, the degradation percentage of methylene blue dye increased and then it started to decline (Fig. 10). Significant decline occurred in the first 60 min, then increased until 120 min, when equilibrium was reached. After 120 min, the percentage of degradation was again reduced since the concentration of dye in the solution decreased with increasing time [26].

Trapping experiment: Experiments employing the active species trapping assist explain photocatalyst degradation. The photocatalytic degradation involves several photogenerated species, including h^+, $(OH^\bullet)$ and $(O_2^{\bullet -})$ Scavengers that can trap h^+, $(OH^\bullet)$ and $(O_2^{\bullet -})$ include ethylenediaminetetraacetic acid (EDTA), *p*-benzoquinone (BQ) and isopropyl alcohol (IPA). To elucidate the mechanistic pathways involved in the photo-

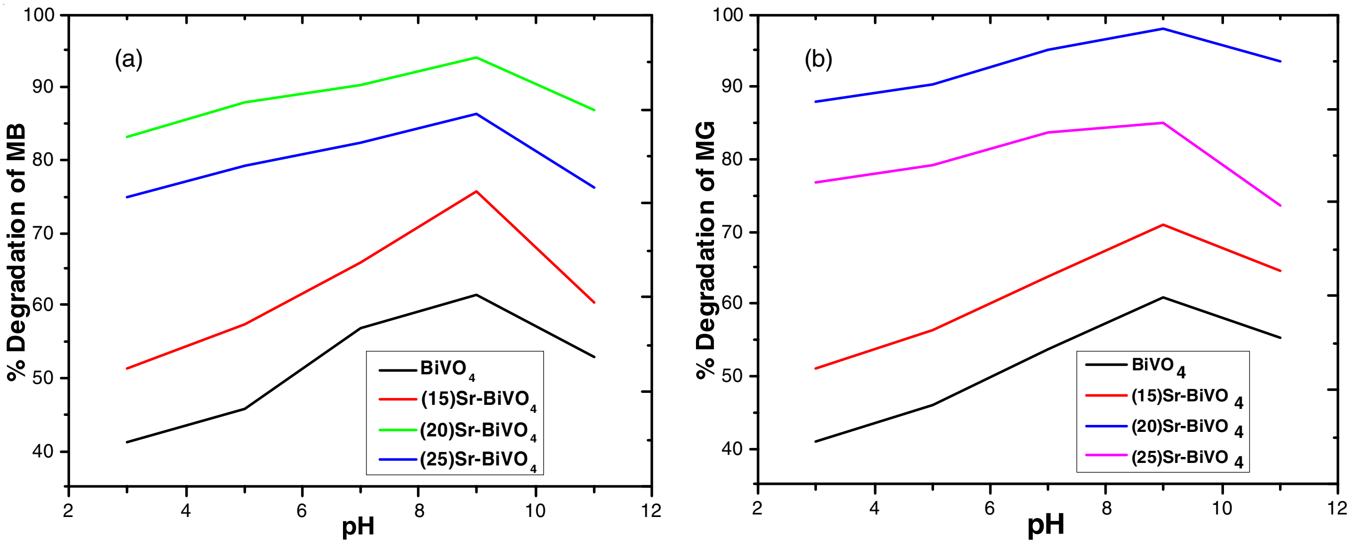

Fig. 8. Photocatalytic degradation of methylene blue (a) and malachite green (b) by undoped $BiVO_4$ and Sr-doped $BiVO_4$ at various wt.% and pH

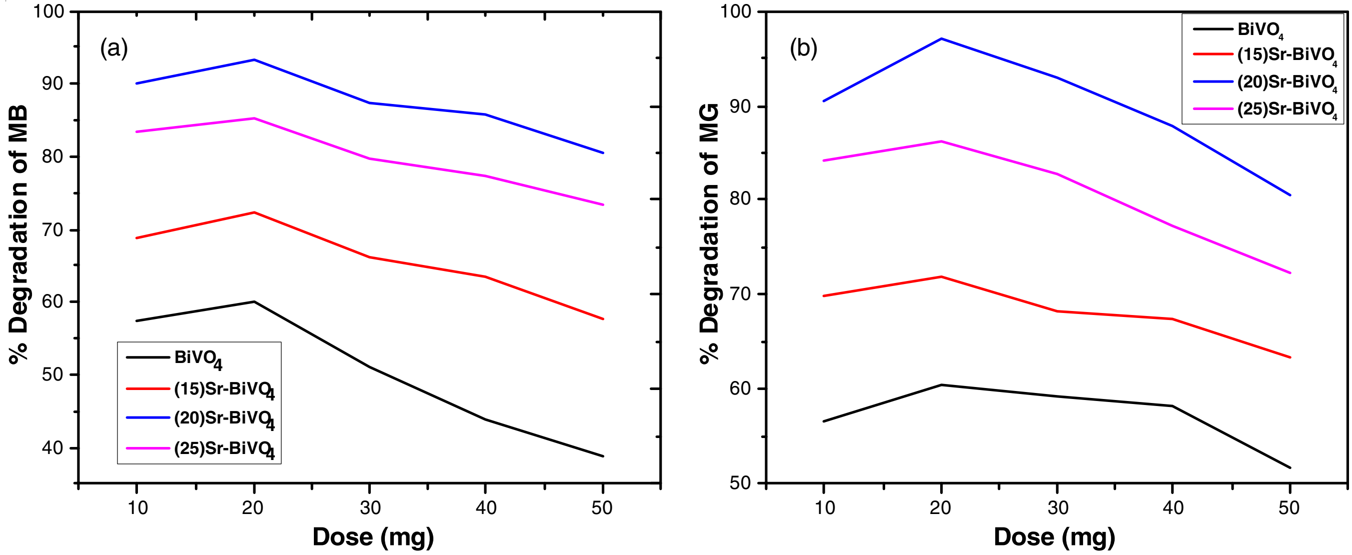

Fig. 9. Photocatalytic degradation of methylene blue and malachite green *vs*. dose (mg)

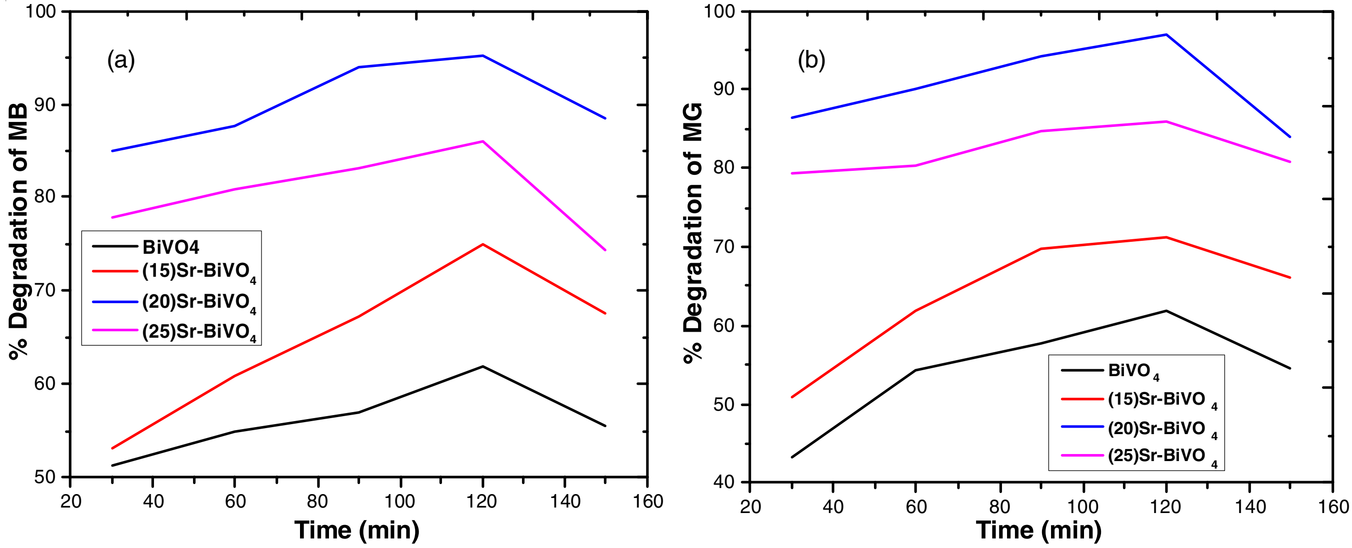

Fig. 10. Photocatalytic degradation of methylene blue (a) and malachite green (b) with changing time

catalytic degradation of methylene blue (MB) and malachite green (MG) dyes by Sr-$BiVO_4$ composite, which demonstrated the highest degradation efficiency, reactive species trapping experiments were conducted. The degradation rates of methylene blue (MB) and malachite green (MG) rapidly decrease with the addition of BQ, a $O_2^{\bullet-}$) scavenger, highlighting the significant role of ($O_2^{\bullet-}$) photogenerated charge carriers in the photocatalytic mechanism. Conversely, the presence of EDTA for h^+ trapping did not affect the efficiency of dye degradation. Moreover, the inclusion of IPA as an ($OH^\bullet$) scavenger slightly hinders the photocatalytic dye degradation indicating that $OH^\bullet$ plays a minor role in the process. These findings (Fig. 11) collectively suggest that ($O_2^{\bullet-}$) predominantly drives the degradation of dyes in this system [27].

Advanced oxidation processes (AOPs) produce highly reactive oxygen species (ROS) with high oxidising ability, such as $OH^\bullet$, $O_2^{\bullet-}$, h^+ and $HO_2^\bullet$. These species can oxidize organic contaminants to CO_2 and inorganic ions, reduce inorganic

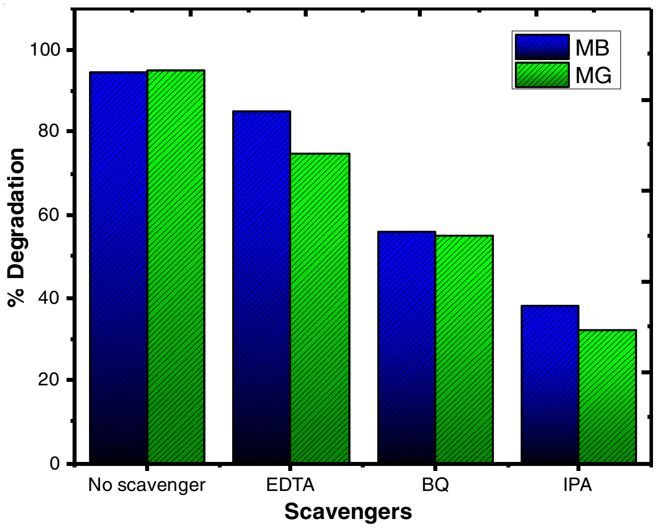

Fig. 11. Influence of reactive species scavengers on the photocatalytic degradation of methylene blue and malachite green

contaminants to non-toxic ions and inactivate microorganisms that produce no noxious compounds [45]. The holes in the valence band react with water and forms hydroxyl radical, which degrades the dye molecule. The transfer of electron from CB of one catalyst to other reduces the electron hole recombination and helps in increasing the photocatalytic activity [46]. The possible photodegradation mechanism of meatl doped bismuth vanadate is shown in Fig. 12.

$$O_2 + e^- \,(CB) \longrightarrow O_2^{\bullet -} \qquad (3)$$

$$h^+(VB) + H_2O \longrightarrow OH^{\bullet -} + H^+ \qquad (4)$$

$$MB/MG + O_2^{\bullet -} + OH^{\bullet} \longrightarrow H_2O + CO_2 \qquad (5)$$

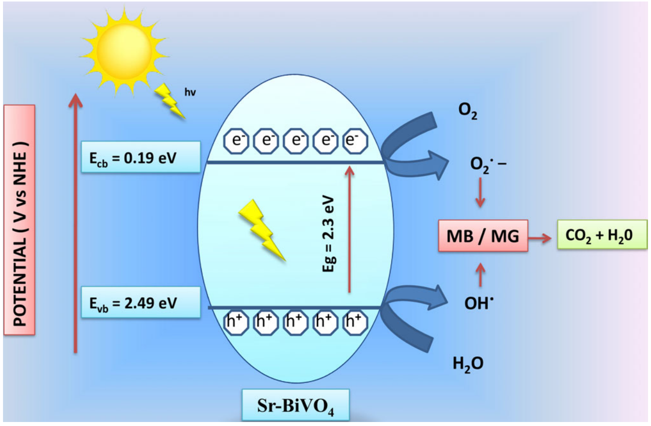

Fig. 12. Mechanism of photocatalysis for the degradation of methylene blue and malachite green by Sr-doped BiVO$_4$

Kinetic study of photocatalytic degradation: The investigation into the degradation rates of methylene blue (MB) and malachite green (MG) dyes under light exposure, catalyzed by BiVO$_4$ and (20)Sr-BiVO$_4$, follows a pseudo-first-order kinetics (eqn. 4):

$$Kt = \ln \frac{C_0}{C} \qquad (4)$$

where K represents the pseudo-first-order rate constant; t signifies time; and C and C_0 denote the dye concentrations at time 't' and at the initial point (t = 0), respectively. The graphs illustrate a linear correlation between the natural logarithm of the initial concentration to the concentration at time 't' $\ln(C_0/C)$ and the duration of light exposure, displaying a positive slope that corresponds to the first-order kinetic model [45] (Fig. 13).

Reusability studies: To demonstrate the efficiency after five runs, the stability and recyclability of the prepared photocatalyst were examined. After every cycle, the analysis were performed in the same conditions as previously indicated. Following each photocatalytic run, the catalysts were separated by filtration and meticulously washed with deionized water to remove any residues, ensuring their readiness for the next cycle of use. Following reusability experiments, in which the photodegradation efficiencies of the Sr-Doped BiVO$_4$ sample in five continuous cycles were examined. Even after five recycles, the catalyst still showed excellent reusability, with no discernible decrease in degrading efficiency (Fig. 14).

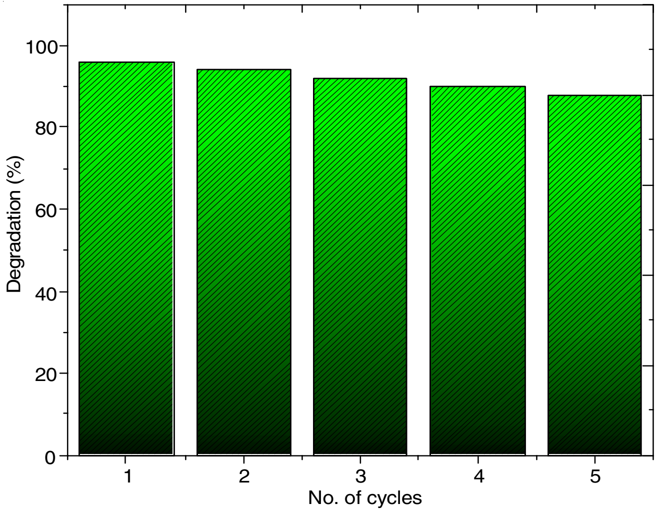

Fig. 14. Reusability of (20)Sr-doped BiVO$_4$ for methylene blue and malachite green photo degradation for five cycles

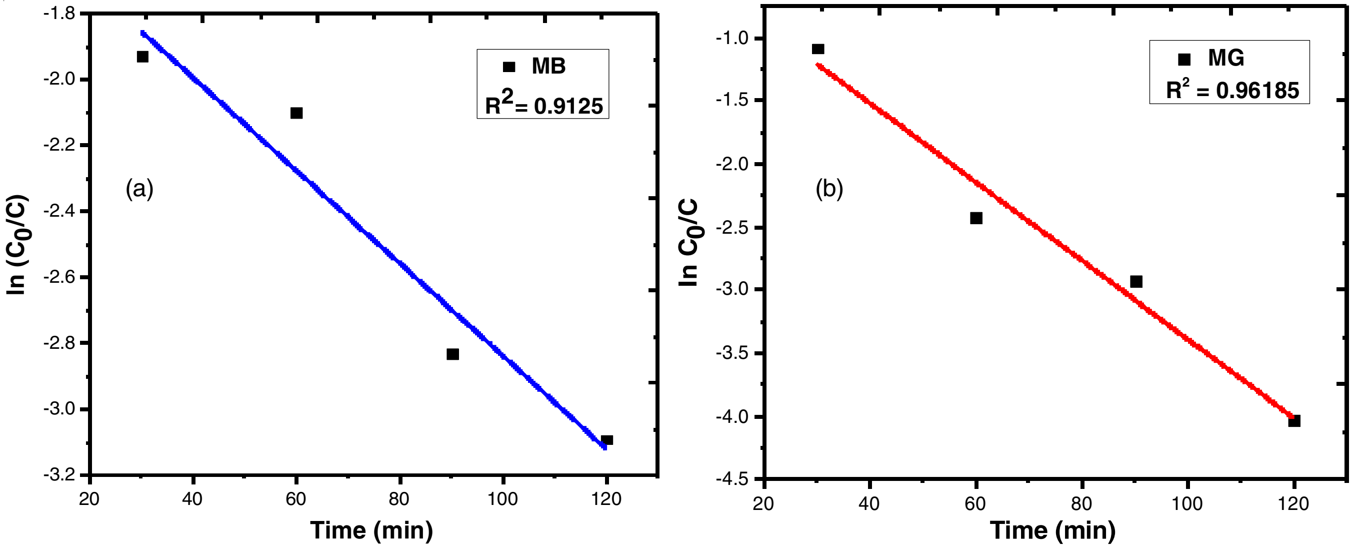

Fig. 13. Pseudo-first order kinetics followed by photo degradation of methylene blue (a) and malachite green (b) by (20)Sr-doped BiVO$_4$

Fig. 15 illustrates the absorption of solar energy by $BiVO_4$ photocatalyst, characterized by a band gap energy of 2.3 eV. The charge separation of e^-/h^+ during photo-excitation creates holes in the valence band (h^+). The hydroxyl radicals ($OH^{\bullet}$) that are produced when water reacts with the photo-induced holes in the valence band have a potent oxidizing effect. Degradation occurs when dye molecules close to the $BiVO_4$ surface are attacked by OH radicals. Anionic superoxide radical ($O_2^{\bullet-}$) is formed simultaneously when oxygen absorbs electrons from the conduction band (e^-). After being protonated, the produced superoxide ($O_2^{\bullet-}$) radicals produce hydroperoxyl radicals ($HO_2^{\bullet}$) and H_2O_2, which again separate to produce reactive hydroxyl radicals ($OH^{\bullet}$) [22]. Thus, the present work demonstrated an improved photodegradation efficiency in a shorter time [26,47-52].

Modifications to $BiVO_4$: By enhancing band-gap or charge separation characteristics, composite synthesis with $BiVO_4$ boosts the photocatalytic activity [23]. The literatures reported in Table-1 can be observed with different modification of $BiVO_4$ and their efficiencies on various toxic dyes.

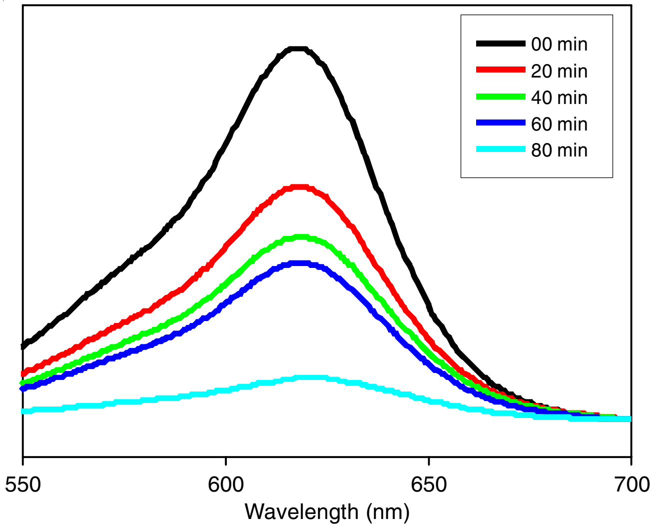

Fig. 15. Decrease in absorbance of methylene blue and malachite green with increasing time

Conclusion

The $BiVO_4$ photocatalyst, synthesized through a facile and economical method, demonstrated exceptional performance, was characterized using UV-DRS, FTIR, FE-SEM and XRD to identify its crystal structure and the optical characteristics. The findings demonstrated that the nanoparticles had retained their structure and were homogeneous. The ability of the produced catalyst to degrade methylene blue and malachite green dyes was used to assess its effectiveness in photocatalytic applications. The results shown that the highest degradation percentages of 95.3% and 96.9% were reached, respectively, for methylene blue and malachite green dyes with (20)Sr-$BiVO_4$ under sunlight irradiation for 120 min at pH 9 and at the catalyst dose of 0.20 g.

ACKNOWLEDGEMENTS

The authors are grateful to the Department of Chemistry, ITER, Siksha 'O' Anusandhan (Deemed to Be University), Bhubaneswar, India for providing the research facilities. Thanks are also due to Material Analysis & Research Centre, Bengaluru, India for carrying out the BET analysis within the required time.

CONFLICT OF INTEREST

The authors declare that there is no conflict of interests regarding the publication of this article.

REFERENCES

1. M. Bodzek and M. Rajca, *Ecol. Chem. Eng. S*, **19**, 489 (2012); https://doi.org/10.2478/v10216-011-0036-5
2. S.S. Shinde, C.H. Bhosale and K.Y. Rajpure, *J. Photochem. Photobiol. B*, **103**, 111 (2011); https://doi.org/10.1016/j.jphotobiol.2011.02.002

TABLE-1
EFFICIENCIES AND APPLICATIONS OF MODIFIED $BiVO_4$

Metal- doped	Synthesis	Band gap	Light source	Time (min)	Dyes	Degradation (%)	Ref.
Ag/Yt co- doped $BiVO_4$	Solid-state reaction	1.65	Solar-light	120	Crystal violet	94.57	[53]
Au-loaded $BiVO_4$	Hydrothermal	2.39	Visible light	60	Crystal violet	98.21	[28]
Pt- doped $BiVO_4$	Hydrothermal	1.99	Visible light	180	Methylene blue	92	[54]
Co-doped $BiVO_4$	Heteronuclear complexing	2.42	Solar light	30	Methylene blue	85	[55]
Ni-doped $BiVO_4$	Hydrothermal	2.37	Visible light	75	Rhodamine B	96	[56]
Ag/La co-doped $BiVO_4$	Hydrothermal	2.24	Sunlight	180	Xylenol orange & rhodamine B	93 and 95	[57]
Gd/Y co-doped $BiVO_4$	Hydrothermal	2.81	Simulated sunlight	90	Methylene blue	94	[58]
Cu-doped $BiVO_4$	Microwave hydrothermal	2.38	Visible light	150	Methylene Blue	95	[59]
Co-doped $BiVO_4$	Microwave hydrothermal	2.28	Visible light	90	Malachite green	99	[60]
Ag-loaded $BiVO_4$	Microwave hydrothermal	2.43	Visible-light-	180	Methylene blue and rhodamine B	99.54 and 98.49	[61]
Tb-doped $BiVO_4$	Hydrothermal	2.29	Visible light	150	Methylene blue	98.2	[62]
Mo-doped $BiVO_4$	Combustion	3.71	Visible light	120	Malachite green	99	[63]
Pd-doped $BiVO_4$	Microwave-assisted	2.27	Visible-light	150	Malachite green	98	[64]
Al- doped $BiVO_4$	Hydrothermal	2.44	Visible light	90	RhB	96	[65]
	Co-precipitation	2.3	Stimulated sunlight	120	Methylene blue & malachite green	95.3 and 96.9	Present study

3. F. Li, C. Yang, Q. Li, W. Cao and T. Li, *Mater. Lett.*, **145**, 52 (2015); https://doi.org/10.1016/j.matlet.2015.01.043
4. C.P. Sajan, S. Wageh, A.A. Al-Ghamdi, J. Yu and S. Cao, *Nano Res.*, **9**, 3 (2016); https://doi.org/10.1007/s12274-015-0919-3
5. C. Xia, S.W. Joo, A. Hojjati-Najafabadi, H. Xie, Y. Wu, T. Mashifana and Y. Vasseghian, *Chemosphere*, **329**, 138580 (2023); https://doi.org/10.1016/j.chemosphere.2023.138580
6. V. Pratap Singh and R. Vaish, *Constr. Build. Mater.*, **234**, 117377 (2020); https://doi.org/10.1016/j.conbuildmat.2019.117377
7. T. Robinson, G. Mc Mullan, R. Marchant and P. Nigam, *Bioresour. Technol.*, **77**, 247 (2001); https://doi.org/10.1016/S0960-8524(00)00080-8
8. E. Issaka, E. Danso-Boateng and J. Baffoe, Desalin. Water Treatment, 319, 100574 (2024); https://doi.org/10.1016/j.dwt.2024.100574
9. A. Hojjati-Najafabadi, E. Farahbakhsh, G. Gholamalian, F. Davar, T.M. Aminabhavi, P. Feng, Y. Vasseghian, H. Kamyab and H. Rahimi, *J. Water Process Eng.*, **59**, 105002 (2024); https://doi.org/10.1016/j.jwpe.2024.105002
10. C. Yu, Z. Xue, Y. Mao, J.F. Huang, F. Tao, Z. Cai, C. Fan and L. Pei, *Curr. Mater. Sci.*, **15**, 142 (2022); https://doi.org/10.2174/2666145414666211125094817
11. B.S. Kalanoor, H. Seo and S.S. Kalanur, *Mater. Sci. Energy Technol.*, **4**, 317 (2021); https://doi.org/10.1016/j.mset.2021.08.010
12. K. Shantha and K.B.R. Varma, *Mater. Sci. Eng. B*, **60**, 66 (1999); https://doi.org/10.1016/S0921-5107(99)00021-5
13. L. Ren, L. Jin, J.-B. Wang, F. Yang, M.-Q. Qiu and Y. Yu, *Nanotechnology*, **20**, 115603 (2009); https://doi.org/10.1088/0957-4484/20/11/115603
14. S. Tokunaga, H. Kato and A. Kudo, *Chem. Mater.*, **13**, 4624 (2001); https://doi.org/10.1021/cm0103390
15. A.R. Lim, S.H. Choh and M.S. Jang, *J. Phys. Condens. Matter*, **7**, 7309 (1995); https://doi.org/10.1088/0953-8984/7/37/005
16. L. Zhou, W. Wang, L. Zhang, H. Xu and W. Zhu, *J. Phys. Chem. C*, **111**, 13659 (2007); https://doi.org/10.1021/jp065155t
17. A. Walsh, Y. Yan, M.N. Huda, M.M. Al-Jassim and S.-H. Wei, *Chem. Mater.*, **21**, 547 (2009); https://doi.org/10.1021/cm802894z
18. M.M. Sajid, N. Amin, N.A. Shad, S.B. Khan, Y. Javed and Z. Zhang, *Mater. Sci. Eng. B*, **242**, 83 (2019); https://doi.org/10.1016/j.mseb.2019.03.012
19. M. Long, W. Cai, J. Cai, B. Zhou, X. Chai and Y. Wu, *J. Phys. Chem. B*, **110**, 20211 (2006); https://doi.org/10.1021/jp063441z
20. K. Hirota, G. Komatsu, M. Yamashita, H. Takemura and O. Yamaguchi, *Mater. Res. Bull.*, **27**, 823 (1992); https://doi.org/10.1016/0025-5408(92)90177-2
21. Y. Geng, P. Zhang and S. Kuang, *RSC Adv.*, **4**, 46054 (2014); https://doi.org/10.1039/C4RA07427K
22. Y. Shen, M. Huang, Y. Huang, J. Lin and J. Wu, *J. Alloys Compd.*, **496**, 287 (2010); https://doi.org/10.1016/j.jallcom.2010.01.144
23. A. Hooda, P. Rawat and D. Vaya, *Curr. Nanosci.*, **19**, 697 (2023); https://doi.org/10.2174/1573413718666220509130006
24. X. Wang, Z. Sun, F. Tao, X. Zhang and L. Pei, *Curr. Mater. Sci.*, **17**, 167 (2024); https://doi.org/10.2174/2666145416666230302114712
25. B. Guan, J. Chen, Z. Li, Z. Zhuang, Y. Chen, Z. Ma, J. Guo, J. Guo, C. Zhu, X. Hu, S. Zhao, H. Dang, L. Chen, K. Shu, Z. Guo, K. Shi, Y. Li, C. Yi, J. Hu and Z. Huang, *Energy Fuels*, **38**, 806 (2024); https://doi.org/10.1021/acs.energyfuels.3c03932
26. K. Ji, Hongxing Dai, J. Deng, H. Zang, H. Arandiyan, S. Xie and H. Yang, *Appl. Catal. B: Environ.*, **168-169**, 274 (2015); https://doi.org/10.1016/j.apcatb.2014.12.045
27. A.M. Mohammed, F. Aziz, S.S. Mohtar, S.A. Mhamad, B. Ahmadu, M.U. Nasir, K.Y. Muhammad and M. Aziz, *Sustain. Water Resour. Manag.*, **9**, 88 (2023); https://doi.org/10.1007/s40899-023-00868-5
28. N. Khan, F. Stelo, G.H.C. Santos, L.M. Rossi, R.V. Gonçalves and H. Wender, *Appl. Surf. Sci. Adv.*, **11**, 100289 (2022); https://doi.org/10.1016/j.apsadv.2022.100289
29. K. Wannakan, K. Khansamrit, T. Senasu and S. Nanan, *ACS Omega*, **8**, 4835 (2023); https://doi.org/10.1021/acsomega.2c07020
30. Q. Pan, K. Yang, G. Wang, D. Li, J. Sun, B. Yang, Z. Zou, W. Hu, K. Wen and H. Yang, *Chem. Eng. J.*, **372**, 399 (2019); https://doi.org/10.1016/j.cej.2019.04.161
31. M. Guo, Y. Wang, Q. He, W. Wang, W. Wang, Z. Fu and H. Wang, *RSC Advances*, **5**, 58633 (2015b); https://doi.org/10.1039/C5RA07603J
32. C.V. Reddy, K.R. Reddy, N.P. Shetti, J. Shim, T.M. Aminabhavi and D.D. Dionysiou, *Int. J. Hydrogen Energy*, **45**, 18331 (2020); https://doi.org/10.1016/j.ijhydene.2019.02.109
33. L.T.B. Mendonça and W.M. de Azevedo, *J. Mol. Struct.*, **1315**, 138960 (2024); https://doi.org/10.1016/j.molstruc.2024.138960
34. V. Sivakumar, R. Suresh, K. Giribabu and V. Narayanan, *Cogent Chem.*, **1**, 1074647 (2015); https://doi.org/10.1080/23312009.2015.1074647
35. V.I. Merupo, S. Velumani, A. Kassiba and M.A. Garcia-Sanchez, 11th International Conference on Electrical Engineering, Computing Science and Automatic Control (CCE), IEEE Xplore (2014); https://doi.org/10.1109/ICEEE.2014.6978299
36. M.F. Rahman, M.S. Haque, M. Hasan and M.A. Hakim, *Trans. Electr. Electron. Mater.*, **20**, 522 (2019); https://doi.org/10.1007/s42341-019-00144-4
37. P. Pookmanee, P. Intaphong and S. Phanichphant, *Adv. Mater. Res.*, **1103**, 85 (2015); https://doi.org/10.4028/www.scientific.net/AMR.1103.85
38. M.S. Mansha and T. Iqbal, *Opt. Quantum Electron.*, **54**, 706 (2022); https://doi.org/10.1007/s11082-022-04114-8
39. L. Geronimo, C.G. Ferreira, V. Gacha, D. Raptis, J. Martorell and C. Ros, *ACS Appl. Energy Mater.*, **7**, 1792 (2024); https://doi.org/10.1021/acsaem.3c02775
40. H. Chen, Q. Zhang, A. Abbas, W. Zhang, S. Huang, X. Li, S. Liu and J. Shuai, *Catalysts*, **13**, 1063 (2023); https://doi.org/10.3390/catal13071063
41. M. Tayebi and B.-K. Lee, *Catal. Today*, **361**, 183 (2021); https://doi.org/10.1016/j.cattod.2020.03.066
42. H.S. Park, K.E. Kweon, H. Ye, E. Paek, G.S. Hwang and A.J. Bard, *J. Phys. Chem. C*, **115**, 17870 (2011); https://doi.org/10.1021/jp204492r
43. A.J. Josephine, C.R. Dhas, R. Venkatesh, D. Arivukarasan, A.J. Christy, S.E. Santhoshi Monica and S. Keerthana, *Mater. Res. Express*, **7**, 015036 (2020b); https://doi.org/10.1088/2053-1591/ab653f
44. L. Mohanty, D. Sundar Pattanayak, R. Singhal, D. Pradhan and S. Kumar Dash, *Inorg. Chem. Commun.*, **138**, 109286 (2022); https://doi.org/10.1016/j.inoche.2022.109286
45. D. Pradhan, E. Falletta and S.K. Dash, *Opt. Mater.*, **135**, 113368 (2023); https://doi.org/10.1016/j.optmat.2022.113368
46. D. Pradhan, N. Nayak, M. Kanar and S.K. Dash, *ChemistrySelect*, **9**, e202400217 (2024); https://doi.org/10.1002/slct.202400217
47. K. Lv, D. Wan, D. Zheng, Y. Qin and Y. Lv, *J. Alloys Compd.*, **872**, 159597 (2021); https://doi.org/10.1016/j.jallcom.2021.159597
48. W. He, X. Zhang, X. Dong, X. Zhang, C. Ma and H. Ma, *J. Adv. Oxid. Technol.*, **17**, 33 (2014); https://doi.org/10.1515/jaots-2014-0104
49. R. Ran, J.G. McEvoy and Z. Zhang, *Int. J. Photoenergy*, **2015**, Article ID 612857 (2015); https://doi.org/10.1155/2015/612857

50. A. Saleem, T. Ahmed, M. Ammar, H. Zhang, H. Xu and R. Tabassum, *J. Photochem. Photobiol. B*, **213**, 112070 (2020); https://doi.org/10.1016/j.jphotobiol.2020.112070
51. M.M. Sajid, N. Amin, N.A. Shad, S.B. Khan, Y. Javed and Z. Zhang, *Mater. Sci. Eng.*, **242**, 83 (2019); https://doi.org/10.1016/j.mseb.2019.03.012
52. L. Zou, H. Wang and X. Wang, *ACS Sustain. Chem.& Eng.*, **5**, 303 (2017); https://doi.org/10.1021/acssuschemeng.6b01628
53. O.P. Kumar, M.N. Ashiq, M. Ahmad, S. Anjum and A.U. Rehman, *J. Mater. Sci. Mater. Electron.*, **31**, 21082 (2020); https://doi.org/10.1007/s10854-020-04620-z
54. M.M. Sajid, H. Zhai, T. Alomayri, S.B. Khan, Y. Javed, N.A. Shad, A.R. Ishaq, N. Amin and Z. Zhang, *J. Mater. Sci. Mater. Electron.*, **33**, 15116 (2022); https://doi.org/10.1007/s10854-022-08431-2
55. B. Zhou, X. Zhao, H. Liu, J. Qu and C. Huang, *Appl. Catal. B*, **99**, 214 (2010); https://doi.org/10.1016/j.apcatb.2010.06.022
56. S. Li, Y. Cheng, Q. Wang, C. Liu and L. Xu, *Mater. Res. Express*, **7**, 115005 (2020); https://doi.org/10.1088/2053-1591/abc79e
57. S. Prabhavathy and D. Arivuoli, *Inorg. Chem. Commun.*,, **141**, 109483 (2022); https://doi.org/10.1016/j.inoche.2022.109483
58. M. Noor, F. Sharmin, M.A. Mamun, S. Hasan, M. Hakim and M. Basith, *J. Alloys Compd.*, **895**, 162639 (2022); https://doi.org/10.1016/j.jallcom.2021.162639
59. C. Regmi, Y.K. Kshetri, R.P. Pandey, T.H. Kim, G. Gyawali and S.W. Lee, *J. Environ. Sci.*, **75**, 84 (2019); https://doi.org/10.1016/j.jes.2018.03.005
60. C. Regmi, T.H. Kim, S.K. Ray, T. Yamaguchi and S.W. Lee, *Res. Chem. Intermed.*, **43**, 5203 (2017); https://doi.org/10.1007/s11164-017-3036-y
61. C. Regmi, D. Dhakal and S.W. Lee, *Nanotechnology*, **29**, 064001 (2018); https://doi.org/10.1088/1361-6528/aaa052
62. W.S. Chen, M.H. Wu and J.Y. Wu, *Sustainability*, **15**, 6994 (2023); https://doi.org/10.3390/su15086994
63. V.G. Warrier, J. Devasia, A. Nizam and G. Nagendra, *Int. J. Environ. Anal. Chem.*, **104**, 3314 (2024); https://doi.org/10.1080/03067319.2022.2085039
64. D. Channei, P. Thammaacheep, S. Kerdphon, W. Khanitchaidecha, P. Jannoey and A. Nakaruk, *Inorg. Chem. Commun.*, **150**, 110478 (2023); https://doi.org/10.1016/j.inoche.2023.110478
65. S. Zhang, X. Ou, X. Yang, D. Wang and C. Zhang, *Chem. Phys. Lett.*, **778**, 138747 (2021); https://doi.org/10.1016/j.cplett.2021.138747